Water Resources Research

RESEARCH ARTICLE
10.1029/2022WR033686

Special Section:
Modeling, simulation, and big data techniques in subsurface fluid flow and transport

Pore-Scale Determination of Residual Gas Remobilization and Critical Saturation in Geological CO_2 Storage: A Pore-Network Modeling Approach

Ramin Moghadasi[1,2], Sajjad Foroughi[2], Farzad Basirat[1], Steven R. McDougall[3], Alexandru Tatomir[4], Branko Bijeljic[2], Martin J. Blunt[2], and Auli Niemi[1]

[1]Department of Earth Sciences, Uppsala University, Uppsala, Sweden, [2]Department of Earth Science and Engineering, Imperial College, London, UK, [3]Institute of GeoEnergy Engineering, Heriot-Watt University, Edinburgh, UK, [4]Department of Applied Geology, University of Göttingen, Göttingen, Germany

Key Points:

- Remobilization of residually trapped gas occurs at a higher saturation than residual saturation, called the critical gas saturation
- Ostwald ripening tends to slightly increase the mobilization saturation
- The relative permeability of remobilized gas is significantly reduced, which adds to the security of residual trapping

Supporting Information:

Supporting Information may be found in the online version of this article.

Correspondence to:

R. Moghadasi,
ramin.moghadasi@geo.uu.se;
r.moghadasi@imperial.ac.uk

Citation:

Moghadasi, R., Foroughi, S., Basirat, F., McDougall, S. R., Tatomir, A., Bijeljic, B., et al. (2023). Pore-scale determination of residual gas remobilization and critical saturation in geological CO_2 storage: A pore-network modeling approach. *Water Resources Research*, *59*, e2022WR033686. https://doi.org/10.1029/2022WR033686

Received 14 SEP 2022
Accepted 23 MAY 2023

Author Contributions:

Conceptualization: Ramin Moghadasi
Data curation: Sajjad Foroughi
Formal analysis: Ramin Moghadasi, Farzad Basirat, Martin J. Blunt, Auli Niemi
Funding acquisition: Auli Niemi
Investigation: Ramin Moghadasi, Sajjad Foroughi, Auli Niemi

Abstract Remobilization of residually trapped CO_2 can occur under pressure depletion, caused by any sort of leakage, brine extraction for pressure maintenance purposes, or simply by near wellbore pressure dissipation once CO_2 injection has ceased. This phenomenon affects the long-term stability of CO_2 residual trapping and should therefore be considered for an accurate assessment of CO_2 storage security. In this study, pore-network modeling is performed to understand the relevant physics of remobilization. Gas remobilization occurs at a higher gas saturation than the residual saturation, the so-called critical saturation; the difference is called the mobilization saturation, a parameter that is a function of the network properties and the mechanisms involved. Regardless of the network type and properties, Ostwald ripening tends to slightly increase the mobilization saturation, thereby enhancing the security of residual trapping. Moreover, significant hysteresis and reduction in gas relative permeability is observed, implying slow reconnection of the trapped gas clusters. These observations are safety enhancing features, due to which the remobilization of residual CO_2 is delayed. The results, consistent with our previous analysis of the field-scale Heletz experiments, have important implications for underground gas and CO_2 storage. In the context of CO_2 storage, they provide important insights into the fate of residual trapping in both the short and long term.

1. Introduction

Carbon Capture and Storage (CCS) is one of the key methods to reduce atmospheric emissions of CO_2 and thereby mitigate climate change (IPCC, 2005). In CCS, anthropogenic CO_2 is captured and injected into deep porous underground reservoirs (e.g., saline aquifers), where it can be contained for long periods by various trapping mechanisms (Orr Jr, 2018). The injected CO_2 plume will gradually migrate upwards due to buoyancy forces. At the trailing edge of the plume, however, a fraction of the injected CO_2 is trapped when water re-enters the system as immobile isolated blobs or ganglia due to pore-scale capillary forces (Rasmusson et al., 2018; Tanino & Blunt, 2012). This mechanism is called residual trapping, quantitively defined by the residual saturation (S_{gr}), and serves as a key mechanism for secure geological CO_2 storage (Gershenzon et al., 2014; Krevor et al., 2015; Qi et al., 2009).

In the long term, the residually trapped CO_2 will eventually dissolve into the resident fluid (brine), where there is sufficient contact with fresh brine. This process, which is further accelerated by the density contrast between the fresh and aqueous solution of CO_2, enhances long-term storage. However, in regions where a large amount of residually trapped CO_2 is contained, and the aqueous brine phase is already saturated with CO_2, contact with fresh brine is limited. Moreover, the mixing is prolonged due to the lower density contrast. Therefore, it is crucial to understand how secure the residual trapping is in these regions on various time scales.

Up to now, the short-term (tens of years) effectiveness of CO_2 residual trapping has been extensively studied at various relevant spatial scales. In contrast, its long-term stability is not yet very well understood due to the lack of data. Determining the long-term stability of CO_2 residual trapping requires a deep understanding of the relevant processes and conditions under which the trapped CO_2 can be remobilized.

Pressure depletion is one of the processes by which the remobilization of residually trapped CO_2 can take place. We assume that CO_2 has been injected into an aquifer and allowed to become residually trapped at the tail of the plume. In the event of pressure depletion, residually trapped CO_2 expands, and consequently the CO_2 saturation

Methodology: Ramin Moghadasi, Martin J. Blunt
Resources: Sajjad Foroughi, Alexandru Tatomir
Software: Ramin Moghadasi, Steven R. McDougall
Supervision: Farzad Basirat, Steven R. McDougall, Branko Bijeljic, Martin J. Blunt, Auli Niemi
Validation: Ramin Moghadasi
Visualization: Ramin Moghadasi
Writing – original draft: Ramin Moghadasi
Writing – review & editing: Farzad Basirat, Alexandru Tatomir, Branko Bijeljic, Martin J. Blunt, Auli Niemi

increases. In addition, CO_2 also exsolves from the aqueous phase, thereby adding to the volume of the gas-phase CO_2 (Huber et al., 2018; Zuo et al., 2012). Eventually, the trapped CO_2 ganglia grow and can then reconnect to become mobile again. Causes for a decline in reservoir pressure could be any type of leakage (a leaky wellbore or a fracture) or simply dissipation of pressure build-up near a wellbore (Jiang et al., 2014; Shi et al., 2013). Common examples of leakage are due to impairments in the wellbore cement or downhole completion equipment or a fracture, which can occur due to underground movement along an existing fault line. Figure 1 provides a schematic of how trapped CO_2 may remobilize if the reservoir pressure drops.

The effect of pressure depletion on the remobilization of trapped gas, also referred to as depressurization, was first studied within the oil and gas industry in the context of minimizing the gas-oil ratio during oil production in gas condensate reservoirs and for natural gas storage (Ahmed et al., 1998; Drummond et al., 2001; Fevang & Whitson, 1996; Fishlock et al., 1988; Naylor et al., 2000; Raghavan & Jones, 1996). These investigations showed that during pressure depletion, the gas (or CO_2) flows only once its saturation reaches a so-called critical value (denoted by S_{gc}) which can be higher than the residual saturation S_{gr} (Egermann et al., 2010; Egermann & Vizika, 2000; Fishlock et al., 1988). In other words, a higher CO_2 saturation is needed to remobilize the gas phase than if gas is added by injection. In addition, the subsequent gas relative permeability in such cases is substantially reduced compared to that during waterflooding to trap gas (Egermann et al., 2010; Zuo et al., 2012, 2013).

In the past, the critical gas saturation was probed at the laboratory scale (on centimetre-sized rock samples) using complex experimental procedures. In these protocols, the remobilization of the gas is typically inferred from flow measurements. These experiments can give misleading results due to pore-scale viscous fingering caused by the low viscosity of the gas phase, which lead to an underestimate of S_{gc}. Moreover, in these experiments the salient pore-scale physics of the trapped gas remobilization remains unknown.

In recent years, advances in micro tomography (often called micro-CT) have allowed the direct pore-scale measurement and determination of critical gas saturation at pressure and temperature conditions representative of deep underground reservoirs, and several investigators have addressed the phenomenon for oil and gas systems. Al-Masri and Shapiro (2021) designed an apparatus with X-ray micro-CT with an inline viscometer apparatus and were able to measure critical gas saturation and relative permeability for low permeability rocks under pressure depletion. Berg et al. (2020) determined S_{gc} for a hydrocarbon model system in sandstone by direct measurements using micro-CT imaging. Similarly, Egermann and Vizika (2000) measured S_{gc} under different operating conditions. Reported laboratory scale values of the critical gas saturation range from 0.5% to 50% depending on factors such as rock and fluids properties and the experimental procedure.

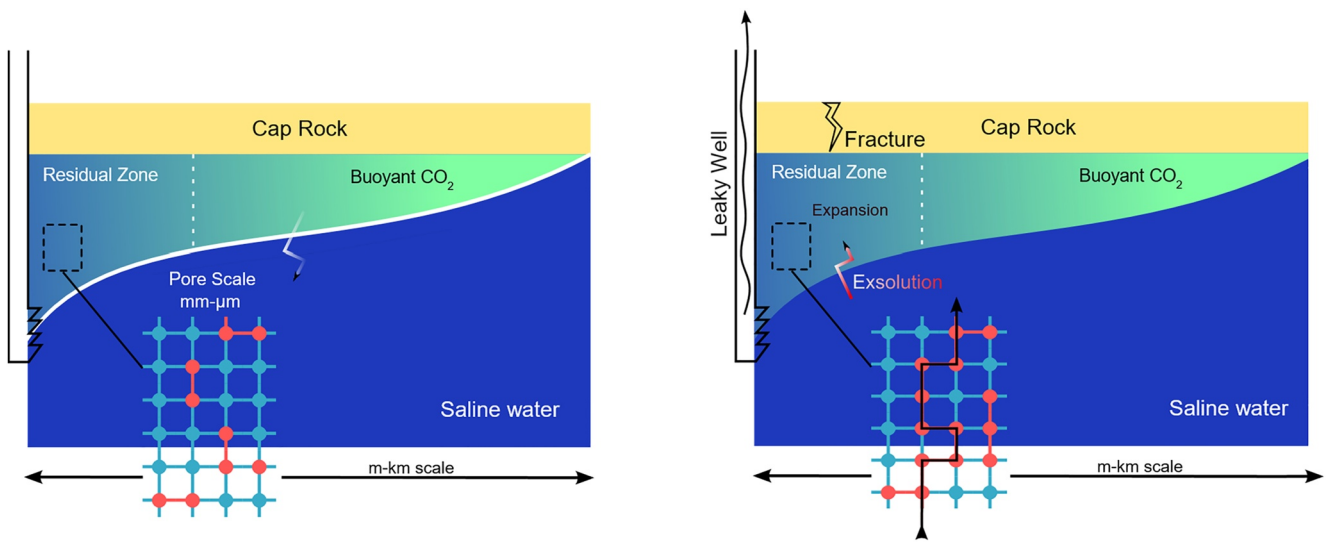

Figure 1. Simple schematic representing residual trapping and trapped gas remobilization under pressure depletion. The possible causes of pressure depletion could be a leaky wellbore, a fracture, or simply pressure dissipation once the injection has stopped. A combination of these is also possible. Left: CO_2 is residually trapped. Right: The pressure decreases once injection ceases. CO_2 saturation increases through expansion and exsolution.

To complement experimental studies, researchers have suggested the use of pore-scale modeling as an effective way to investigate pore-scale processes. Among the available methods, pore network modeling (PNM) is an efficient tool to explore the flow properties within geometrically and topologically representative networks of rock samples at the pore-scale (Blunt, 2001; Ramstad et al., 2019). Typically, a pore network model consists of a network of interconnected pores, which represent the larger voids of the pore space. The connection pathways are referred to as throats and represent the narrower regions between the pores.

The first pore-scale model of depressurization was developed by Li and Yortsos (1995a,b). They provided a detailed analysis of bubble nucleation, growth and reconnection, albeit on a simple network. McDougall and Sorbie (1999) extended this research to develop a pore-scale simulator that can accommodate an irregular 3D lattice. Following that work, several groups have further developed pore-network simulators of the depletion process, most of which were applied for enhanced oil recovery (Bagudu et al., 2018; Bondino et al., 2002, 2003; Ezeuko et al., 2010). However, in a few studies, CO_2 has been considered as the gas phase. For instance, Bagudu et al. (2015) used PNM to investigate the CO_2 migration processes driven by capillary and gravity forces while considering CO_2 dissolution. They estimated S_{gc} under different depletion conditions; however, they did not consider the remobilization of residually trapped CO_2.

While gas remobilization during pressure depletion is relatively well studied for oil and gas recovery, it has received little attention in the context of CCS. Recently, this phenomenon was observed when interpreting the results of a deep CO_2 field injection experiment at Heletz, Israel, the so-called Heletz Residual Trapping Experiment II (RTE II) (Niemi et al., 2020). The results of the tracer experiment (Joodaki et al., 2020) as well as analysis of the CO_2 self-release period using a coupled wellbore-reservoir simulator (Basirat et al., 2020), could only be interpreted by introducing the concept of critical saturation into the models (Moghadasi et al., 2020). These model interpretations highlighted the importance of gas remobilization in CCS. However, the pore level physics of the residual gas remobilization and factors determining the critical gas saturation are not yet well understood in the context of CO_2 remobilization.

An additional mechanism that potentially renders the residually trapped CO_2 unstable is Ostwald ripening: differences in local capillary pressure lead to slight variations in solubility. The resultant concentration gradients drive a diffusive flux of dissolved gas to equilibrate the capillary pressure. Larger bubbles can grow in size and eventually become remobilized (de Chalendar et al., 2018; Li, Orr, & Benson, 2021). While this process was considered in the original work of Li and Yortsos (1995a,b) it is only more recently that the impact of Ostwald ripening in the context of CCS has been studied. Garing et al. (2017) used a series of multi-scale micro-CT images to show that Ostwald ripening in homogenous rocks does not play an important role in the remobilization of residually trapped gas. However, they noted that Ostwald ripening can cause gas remobilization in heterogenous rocks, in which the differences in capillary pressure between different portions of the rock are significant. Xu et al. (2019) developed a simplified model and demonstrated that residual trapping might not be stable due to the bubbles being redistributed through gravity-induced Ostwald ripening. However, their work neglected the effect of CO_2 dissolution on brine density. Most recently, Mehmani and Xu (2022) developed a fully implicit pore network model to simulate Ostwald ripening that could predict the equilibrium distribution of gas bubble volumes observed in micro-fluidics experiments. They showed that the effect of Ostwald ripening is slower in heterogeneous porous media because the average distance between bubbles increases as the system reaches equilibrium, thereby increasing the time scale at which the molecular diffusion is effective.

Although the previous experimental and modeling research has shed light on the various aspects of gas remobilization in porous media in CCS, they have focused on only one mechanism at a time. In contrast, in reality, several mechanisms coincide and may all contribute to trapped gas remobilization. Due to this fact, the studies to date fall short in addressing the risks/effects associated with the dynamics of remobilized gas, which contributes significantly to the long-term safety of geological CO_2 storage.

To fill this knowledge gap, this work is dedicated to study the pore-level mechanisms associated with the remobilization of trapped CO_2 as a consequence of pressure decline in the aquifer. For this purpose, the pore-network simulator numSCAL, originally developed at Heriot-Watt University (Boujelben, 2017), is modified to account for all the processes involved in trapped gas remobilization, including Ostwald ripening. A series of simulations with 3D networks based on Bentheimer and Heletz sandstones are conducted. The significant advantage of the PNM developed in this work is that it allows us to not only investigate the interplay between different remobilization mechanisms, but also the individual effects of each mechanism. This would be a challenging task in laboratory or field settings.

In the following sections, the text is organized as follows: we first present an overview of the theoretical background of gas (re)mobilization under depletion conditions (Section 2). We then present a summary of the pore-network simulator (Section 2.1). This is followed by a presentation of the models used in this study along with simulation results (Sections 2.2, and 3). The final section, in turn, presents the discussion and conclusions of the work (Sections 4 and 5).

2. Model Description

We use a universal pore-network simulator, numSCAL (Boujelben, 2017). Although numSCAL in its earlier form can model the depletion process, the applications were limited to enhanced oil and gas recovery. Moreover, the simulator did not account for residual gas in the network, which can become mobile during a secondary drainage induced by pressure depletion. Furthermore, the phenomenon of Ostwald ripening was not implemented in this code originally. To address these issues, major modifications were incorporated into the simulator as described below.

2.1. Code Implementation

As a primary modification, the pressure-dependent thermodynamic properties of a system containing brine-CO_2 are incorporated into the numSCAL simulator (see Supporting Information S1). Another development is the ability to account for the existence and remobilization of initially present residually trapped gas. To account for this, prior to the pressure depletion simulation, the model first simulates primary drainage—the injection phase—during which the gas is injected, and water/brine is displaced. Next, waterflooding is simulated, representing the post-injection migration of CO_2 in a storage aquifer, by which the gas becomes residually trapped. Prior to simulating the depletion process, a clustering algorithm is applied on the network, to identify the residual gas clusters. Then, the properties of each cluster are assigned such that local capillary equilibrium is initially satisfied throughout the whole network—this is the Ostwald ripening process. Finally, as the last step, pressure depletion is modeled.

The depletion process in numSCAL is implemented in three steps, which take place sequentially as the pressure decreases gradually. These steps are gas diffusion, gas growth, and gas migration. The thermodynamic properties of both fluids are dynamically updated. The basic algorithms associated with each process are summarized in Tables 1–3. Pressure depletion continues until a spanning gas cluster forms, which is a cluster connected to both the inlet and outlet of the network (see Figure 2). The gas saturation at this point defines the critical gas saturation (S_{gc}). This is a valid definition at small scales or when viscous and gravity gradients are not high enough to trigger trapped gas mobilization, as in this study (Li & Yortsos, 1995a, 1995b). However, at larger scales and under larger viscous and gravity gradients, this definition becomes impractical since spanning gas clusters might not even form under such conditions (Amili & Yortsos, 2006; Tsimpanogiannis & Yortsos, 2004). To identify the growing gas clusters, a clustering algorithm is applied, which checks the individual growth of each gas cluster as well as the coalescence of multiple gas clusters. As the clusters merge together, the multiple clusters are considered as one and the total mass of gas in combined clusters is distributed between the pores on a volume-weighted basis.

In the following, the major steps implemented in the depletion module are explained in more detail.

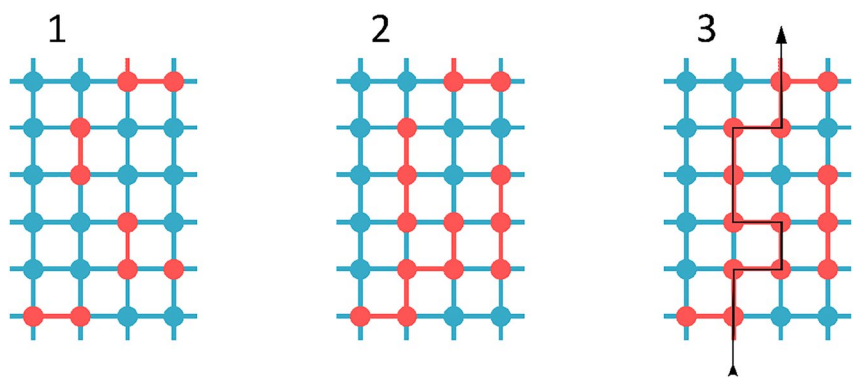

Figure 2. Schematic representation of residual gas evolution during pressure depletion: from 1 to 3, initially, several residual gas clusters (red) exist in the network. As pressure declines, the clusters occupy neighboring pores and therefore grow in size. A network-spanning gas cluster indicates the onset of remobilization.

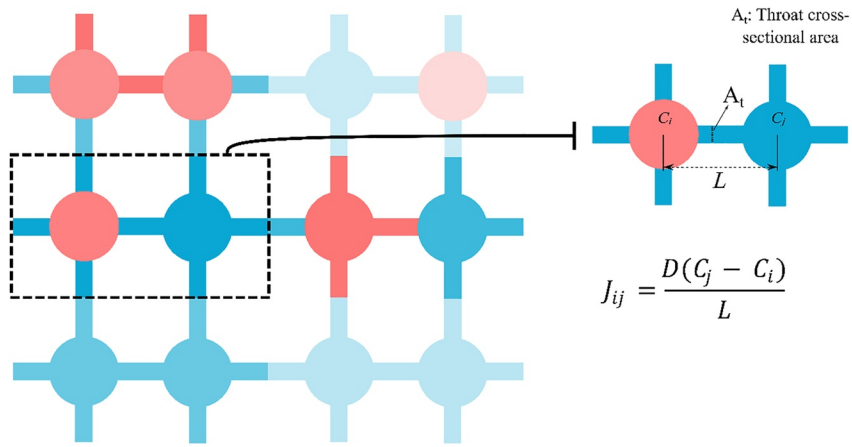

Figure 3. Schematic pore network illustrating the diffusion driven by concentration gradients. The gas-filled and water-filled elements are shown in red and blue, respectively.

Gas diffusion: As long as capillary equilibrium is satisfied the concentration difference is the force that drives the mass diffusion from pore to pore and across the gas-liquid interfaces (see Figure 3). The concentration gradient, in turn transfers the exsolved gas toward the trapped gas bubbles, which act as gas sinks. In the presence of residually trapped gas, these clusters are assumed to be the only gas sinks. The gas fluxes are determined according to Fick's first law:

$$J_{ij} = \frac{D(C_j - C_i)}{L} \tag{1}$$

where J_{ij} denotes the mass flux from pore i to pore j, D is the diffusion coefficient, C_i and C_j are the gas concentrations in pore i, and j respectively, which are determined based on the gas solubility as a function of pressure. L is the effective diffusion length, which is equal to the distance between the centers of pores i and j.

In the numerical code, the gas concentrations are updated by applying a discrete form of Fick's second law applying the mass conservation at each time step:

$$C_i^{new} = C_i^{old} + \frac{(mass_{in}(\Delta t) - mass_{out}(\Delta t))}{V} \tag{2}$$

where $(mass_{in}(\Delta t) - mass_{out}(\Delta t))$ is the net sum of diffusive fluxes across the ends of a pore with volume V. Table 1 gives an overview of the algorithm used to determine gas diffusion.

Table 1
Algorithm for Determining Gas Diffusion

Diffusion algorithm
1. Choose initial diffusion time[a]
If diffusion time < depletion time step[b]
- For every pore i:
→ Apply Fick's law: calculate the inflow and outflow of dissolved gas
→ Update gas concentration in pore i
- Check the conservation of mass in the network
→ If the mass is not conserved, repeat the iteration step with the halved diffusion time
- diffusion time is increased by diffusion time step
Repeat the process until the end of simulation

[a]The choice of the initial diffusion time involves a series of calculations estimating the required diffusion time for each element, the minimum of which is chosen as the initial diffusion time. [b]depletion time step = depletion time (simulation time)/depletion steps. The depletion time step should be finely discretized by choosing large depletion steps (1,000–10,000).

The flux between two neighboring pores takes place across the cross-sectional area of the connecting throat. Therefore, the mass diffusing in time Δt into a pore from a neighboring pore, is calculated by:

$$mass_{in}(\Delta t) - mass_{out}(\Delta t) = \sum_{i \in \aleph} J_i \times A_{ti} \times t_d \quad (3)$$

where $\aleph$ is the set of neighboring pores and A_{ti} is the cross-sectional area of the connecting throat.

As mentioned earlier, diffusion can also be induced by differences in capillary pressures between gas ganglia (de Chalendar et al., 2018). In this process, called Ostwald ripening, gas molecules are redistributed—from ganglia with higher capillary pressures to the ones with lower capillary pressures by molecular diffusion through the aqueous phase—until an equilibrium state of capillary pressure is established. Figure 4a shows two neighboring gas bubbles with unequal capillary pressures. As shown in this figure, the curvature of the interface is smaller in the pore to the right-hand side. According to Laplace's law, the capillary pressure of the bubble to the left is higher than that of the bubble to the right where due to Henry's law there is a lower solubility of gas in the aqueous phase. As a result, gas molecules are transferred from the bubble on the left with higher capillary pressure and solubility to the one on the right, until the capillary pressures are equal (i.e., when the interfacial curvatures of both surfaces are equal). As mass is transferred, the bubble on the left shrinks while the bubble on the right grows. To account for this effect in the modified version of numSCAL, interface gas concentrations are calculated using the pressure

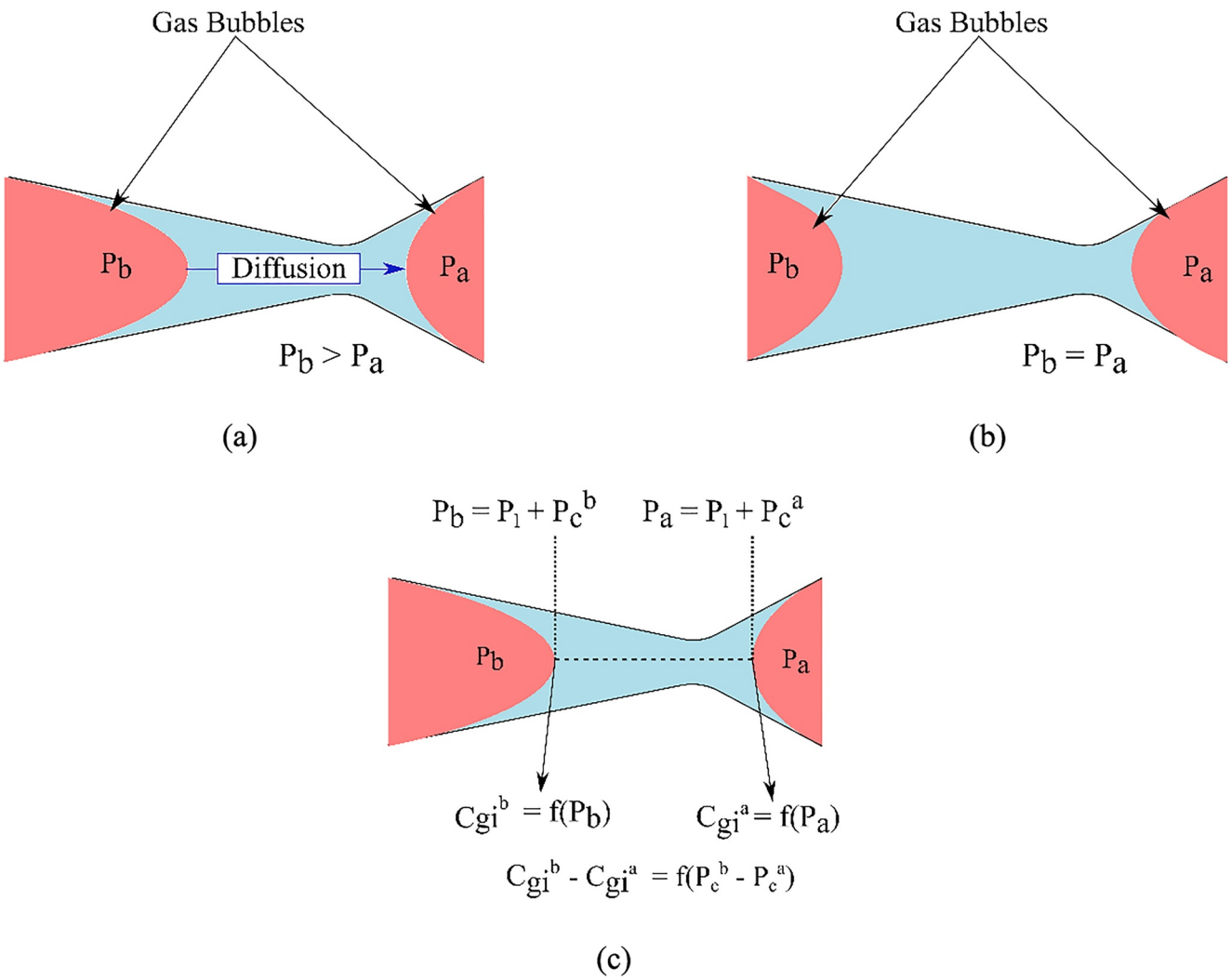

Figure 4. (a–b) Schematic illustration of Ostwald ripening in the pore space where there is a diffusive flux from the bubble on the left to the right to equilibriate the capillary pressure. (c) The boundary conditions at the aqueous phase-gas interfaces.

Table 2
Algorithm for Determining Gas Cluster Growth

Growth algorithm
1. Identify and label gas cluster
2. Calculate the gas pressure for each cluster. An iterative method is applied to estimate the Z factor.
3. At each depletion time step, loop all over the water-filled pores (the wetting phase) adjacent to a gas cluster
- Find the connecting throat j with the minimum entry capillary pressure P_c
- If the internal pressure of the adjacent gas cluster > Pc
• Fill the pore j with gas
• Update the gas cluster volume
• Update the mass in each bubble belonging to the gas cluster
Repeat the process until the end of simulation

inside the bubble, which also takes into account the capillary pressure. This capillary pressure gradient can be then translated into a concentration gradient using Henry's law. Fick's first law can thus be applied to estimate the amount of mass flux between two gas bubbles with unequal capillary pressures.

Figure 4c illustrates the boundary conditions at the gas-aqueous phase interfaces of two bubbles connected via a throat. In this figure, the pressure inside the bubble ($P_{a,b}$) is the sum of aqueous-phase pressure (P_l) and capillary pressure ($P_c^{a,b}$). Note that here the aqueous phase pressure is the same across the throat connecting the two gas bubbles, hence the difference in interfacial gas concentration ($C_{gi}^b - C_{gi}^a$) is a function of the difference in capillary pressures only.

Gas growth: The growth of gas clusters is capillary-controlled. To model this, the volume of each gas cluster is fixed while the corresponding internal gas pressure increases due to both the increase of gas mass through diffusion and the reduction of pressure in the network due to gas compressibility. The gas is allowed to instantly invade the neighboring pore, and therefore expand, once the internal gas pressure exceeds the entry capillary pressure of the connecting throat. A summary of the algorithm implemented in the code to determine gas growth is given in Table 2.

The internal gas pressure is calculated according to the number of moles of gas in a fixed volume of each cluster, which is in turn determined by the volume of elements (pores and throats) occupied. The invasion criteria can be expressed by (Blunt, 2017; Øren et al., 1998):

$$P_g - \left[min\left(P_c^{ij}\right) + P_a\right] = min\left(\Delta P_c^i\right) > 0 \tag{4}$$

where P_g is the internal pressure of the gas phase, P_a is the aqueous phase, and P_c^i is the static equilibrium capillary entry pressure in throat that connects pore i to the neighboring pore j, which can be calculated using equations given in Supporting Information S1. P_g in Equation 4 can be calculated using:

$$P_g = Z(P,T)\, n(t)\, RT/V(t) \tag{5}$$

where Z is the gas compressibility factor, n is the current number of gas moles, R is the universal gas constant, T is temperature, V is the current gas volume, and t is time.

In addition to the above, snap-off in throats is also modeled: this is where water fills the throats potentially disconnecting gas that resides in the neighboring pores. The pressure threshold associated with this event is known as the snap-off capillary pressure, and it refers to the minimum capillary pressure that the fluid-fluid interface can withstand without rupturing (Blunt, 2017). The relevant mathematical formulation can be found elsewhere (refer to Blunt, 2017).

Gas migration: As the size of gas clusters increases, buoyancy forces can become large enough to overcome local capillary forces. As a result, the gas clusters migrate upwards while volume must be conserved. Therefore, the re-imbibition of water, at the bottom of the gas cluster, must be considered. The displacement at the drainage front is determined by the following equation:

$$\Delta P_{Mig}^i = \Delta \rho g h - \frac{2\sigma \cos\theta}{r_i} \tag{6}$$

Table 3
Algorithm for Determining Gas Migration

Migration algorithm
1. At depletion time step, loop all over the water-filled pore adjacent to a gas cluster
- Find the connecting throat j with the minimum entry capillary pressure P_c
- If $P_c < 0$
→ Fill the pore j with gas
→ Update the gas cluster volume
→ Update the mass in each bubble belonging to the gas cluster
2. At depletion time step, loop over all the gas-filled pores of to the invading gas cluster
- Find the connecting throat j with the maximum entry pressure
→ Re-imbibe pore j with the water (wetting phase)
- Repeat, until re-imbibed volume = initially displaced volume
Repeat the process until the end of simulation

where $\Delta\rho$ is the density difference between gas and liquid, h is the height from the bottom of the gas cluster to the neighboring pore i. Re-imbibition of water (the aqueous wetting phase) is modeled following the work of Lenormand and Zarcone (1984). More details are given in Supporting Information S1. The implemented algorithm to determine gas migration is described in Table 3.

2.2. Network Models and Their Properties

In the current study, 3D networks were constructed based on X-ray CT scans of Bentheimer and Heletz sandstones (Niemi et al., 2016; Pore-Scale Modeling Research Group; Tatomir et al., 2016). The Bentheimer network consists of 9484 pores and 21,405 throats, with a porosity of 21.6%, and a permeability of 3,249 mD. The Heletz sandstone is comprised of 18,564 pores and 36,196 throats, with a porosity of 18.2%, and a permeability of 694 mD. Figure 5 shows the extracted pore networks of Bentheimer and Heletz sandstones. Properties of these networks are given in Table 4.

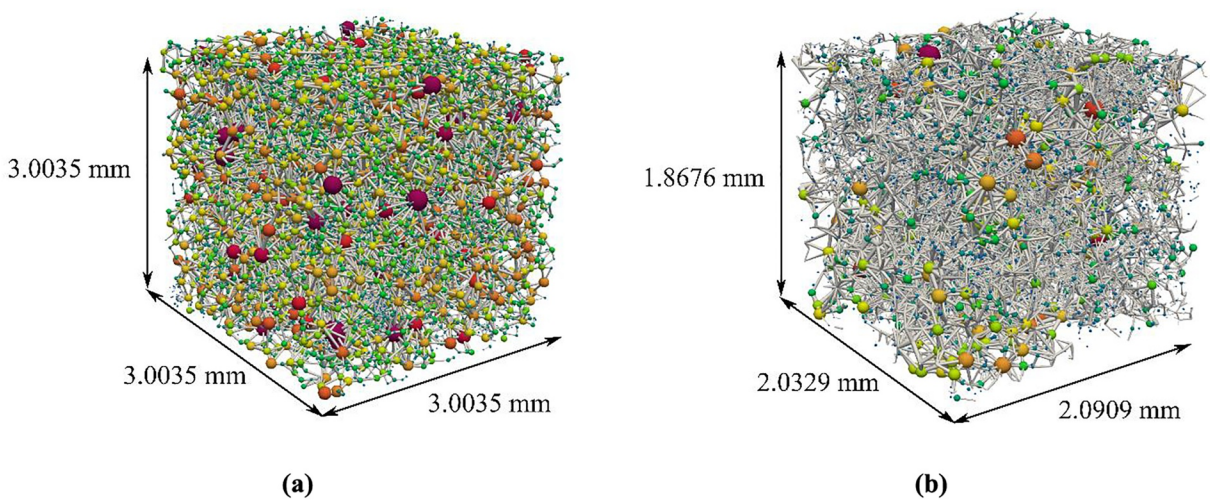

Figure 5. Pore network structure: (a) Bentheimer sandstone, (b) Heletz sandstone. Here, spheres and cylindrical lines schematically represent the pores and throats, respectively.

Table 4
Properties of Networks From X-Ray CT Images

Network name	Porosity %	Permeability mD	Voxel resolution μm	Network dimension (x, y, z) mm
Bentheimer	21.6	3,249	3.0035	3.0035 × 3.0035 × 3.0035
Heletz	18.2	694	9	2.0909 × 2.0329 × 1.8676

2.3. Computational Parameters

In the simulations, one of the main objectives was to analyze the difference between the critical and residual saturation ($S_{gmob} = S_{gc} - S_{gr}$). We refer to the pressure at which mobilization occurs as the critical pressure (P_{crt}). The rest of computational parameters used in the simulations are summarized below.

All depletion simulations are performed at an initial pressure of 24 MPa, at a constant temperature of 60°C, which represents a typical aquifer at an appropriate depth for CO_2 storage (Niemi et al., 2017). The ultimate pressure decline is set to 15 MPa for all simulations. Although this range may not be observed in reality—at the field scale—it was chosen to determine gas relative permeability over a wide range of saturation.

For 3D networks, gravitational effects are taken into account with a gravitational acceleration of 9.8 m/s^2. The thermodynamic properties of the system containing CO_2 and brine/water are determined by accurate correlations available in the literature and are presented in Supporting Information S1. The diffusion coefficient is set to 3.5×10^{-9} m^2/s, neglecting minor changes with respect to pressure (Azin et al., 2013; Cadogan et al., 2014; Z. Li, Orr, & Benson, 2021; Lu et al., 2013). The resident brine is considered as a 5% NaCl in water, with properties corresponding to a brine fully saturated with CO_2. The contact angle is chosen to be 0 indicating a strongly water-wet system.

It should be noted that the gas in the current study is supercritical CO_2, so the terms gas and CO_2 are often used interchangeably throughout the text both referring to supercritical CO_2. Also note that the initial water saturation (S_{wi}), used as an endpoint to both primary and secondary drainage processes, is set to 0.2. This value was chosen to match the core data from Heletz sandstone.

We do not allow new ganglia to nucleate, which can then act as the sites for further nucleation and diffusion. This means that the residually trapped gas clusters are considered to be the only gas sinks to/from which the gas can diffuse. Although this assumption simplifies the model, it is in accordance with earlier findings. Li and Yortsos (1995a) found out that the most plausible mechanism for nucleation in porous media is heterogenous in nature: new bubbles most likely form on the pore walls that contain trapped gas. In other words, the pre-existing gas ganglia swell during pressure depletion but new ganglia do not form.

Since we do not have new nucleation sites, and we always allow the system to reach equilibrium for each increment of pressure decline, the results are independent of the rate of pressure decline: we assume that it is sufficiently slow to allow the concentration to reach equilibrium at the pore scale.

We ignore viscous forces for two reasons: (a) we are principally looking at pressure depletion post injection, where there is little viscous flow; and (b) it has been confirmed both analytically (for idealized simple network geometries) and experimentally (for more complex systems) that the behavior under low rate and stepwise pressure depletion conditions is predominantly capillary-controlled (Kamath & Boyer, 1995). To neglect viscous forces, we impose null pressures at the inlet and outlet of the network as external boundary conditions. The sides are assigned to no-flow conditions.

To ensure computational stability and to accurately capture ganglion growth, the pressure increment is finely discretized. In terms of the processes that are modeled within each pressure step, diffusion is the most time-consuming process, as it requires very small time steps in an explicit scheme for stability. The code initially applies a large timestep for diffusion; however, if the scheme becomes unstable, the timestep is halved and the calculation is repeated. More details can be found at Boujelben (2017). Additionally, the clustering algorithm is optimally decoupled from the diffusion process, which results in higher computational efficiency overall.

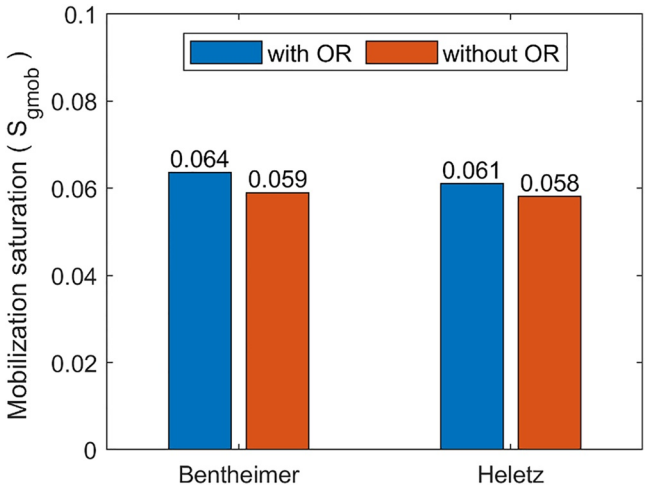

Figure 6. Mobilization saturation (S_{gmob}) for Bentheimer and Heletz pore networks: with and without Ostwald ripening (OR).

3. Results

Primary drainage and imbibition processes are first simulated. The residual gas saturations at the end of imbibition were found to be 0.58, and 0.49 for Bentheimer and Heletz networks, respectively. The high values of residual saturation are associated with the assumption of a zero contact angle and the heterogeneity of the network.

Figure 6 shows that the mobilization saturations are similar for both networks, with values of P_{crt} in the range of 18.5–19.0 MPa. As before, the results show some sensitivity to Oswald ripening; however, the effect is not significant. The same simulations were also repeated in the absence of the gravitational force (i.e., $g = 0$ m/s^2). However, no significant differences were observed, thus the results are not shown here for space considerations.

As noted above, the mobilization saturation S_{gmob} obtained with both networks are similar, despite the fact that the networks represent distinct macroscopic properties—they differ in porosity, permeability, and coordination number. We therefore performed an analysis on their corresponding pore-size distribution (PSD), throat-size distribution (TSD), throat-to-pore aspect ratio (AsR), and coordination number (CN). For each throat of radius R_t, which connects two pores (p_1 and p_2) with radii of R_1 and R_2, respectively, AsR is obtained by $R_l/min\{R_1, R_2\}$; therefore AsR $\in$ (0, 1). The results are presented in Figure 7: the PSD in Heletz network is narrow, while Bentheimer network has a wider PSD. Both networks represent a TSD that is weighted toward values less than 30 μm. On the other hand, they are very similar in terms of AsR and CN. It can, therefore, be hypothesized that flow dynamics under pressure depletion are probably governed by AsR and CN.

Figure 8 shows the simulated gas relative permeability as a function of gas saturation for the entire simulated period including the depletion stage and the previous primary drainage and imbibition. First of all, it can be seen that for both networks, the imbibition curve is slightly higher than the drainage relative permeability, over a range of saturations. This behavior can be attributed to the competing trapping mechanisms at the beginning of imbibition (Spiteri et al., 2008). Focusing on the depletion process, the relative permeability to gas remains zero until the gas saturation reaches S_{gc}, and it then increases rather slowly for the saturations exceeding S_{gc}. This behavior is in agreement with the findings in literature and our previous work (Egermann & Vizika, 2000; Fishlock et al., 1988; Moghadasi et al., 2022). The end point gas relative permeabilities during depletion (i.e., the maximum gas relative permeability) are significantly reduced for both networks, compared to primary drainage. The lower relative permeabilities on reconnection seen here can be explained by the poor connectivity of the gas through the heterogeneous pore space. In Figure 9, the gas phase occupancy within the Heletz network is visualized at the onset of depletion, when the gas is completely trapped, and when it first flows, once a spanning gas cluster is formed. It is evident that a significant portion of the gas remains trapped (shown in red, Figure 9b) even after remobilization, and only a single spanning gas cluster is developed (shown in green, Figure 9b). Furthermore, Figure 9c illustrates that the spanning cluster consists of two distinct clusters connected by a throat of small radius, which explains the low gas permeability of the reconnected gas phase.

4. Discussion

In this study, the evolution of gas mobilization during pressure depletion was investigated by means of pore network modeling with data from Bentheimer and Heletz rocks. Overall, the results showed delayed gas remobilization during pressure depletion: the gas remained immobile beyond values of the residual saturation. The difference, the mobilization saturation, was approximately 0.06 for both of the rocks investigated. This is in agreement with our earlier results from field conditions (Moghadasi et al., 2022) as well as data from oil-gas systems.

Accounting for Ostwald ripening tends to increase the mobilization saturation, but the effect was small. Gas phase reconnection is to some extent delayed by Ostwald ripening. In the context of geological CO_2 storage this means that the remobilization of residually trapped CO_2 is more restricted, and the trapped CO_2 remains trapped for higher saturations. Furthermore, the insignificant effects of the gravity force indicated that gravitational remobilization of the residually trapped CO_2 is exceptionally difficult, which is in agreement with the findings of Andrew et al. (2014).

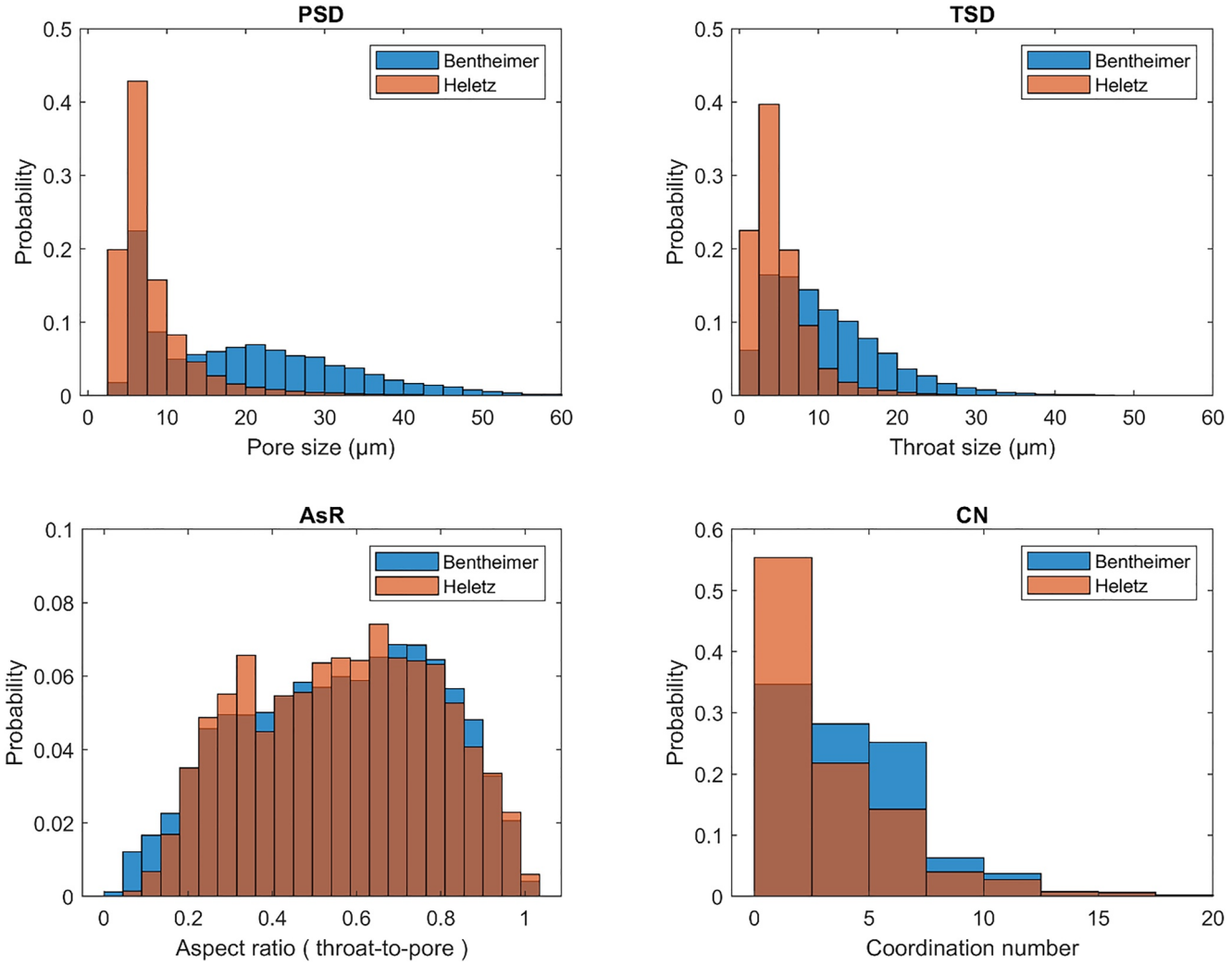

Figure 7. Pore space analysis of Bentheimer and Heletz sandstones. Pore-size distribution (PSD), throat-size distribution (TSD), throat-to-pore aspect ratio (AsR), and coordination number (CN).

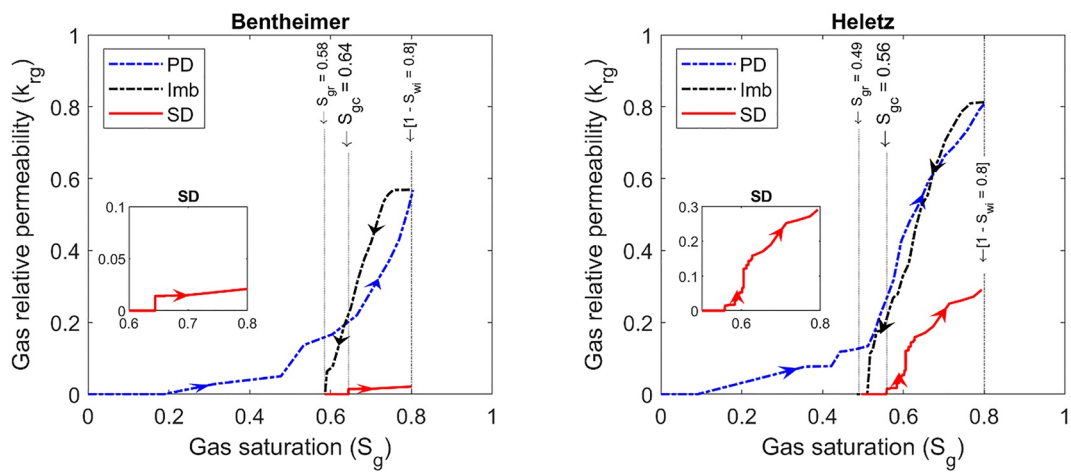

Figure 8. Gas relative permeability (k_{rg}) versus gas saturation (S_g): (left) Bentheimer pore-network, (right) Heletz pore-network. (PD: primary drainage, Imb: Imbibition, SD: secondary drainage).

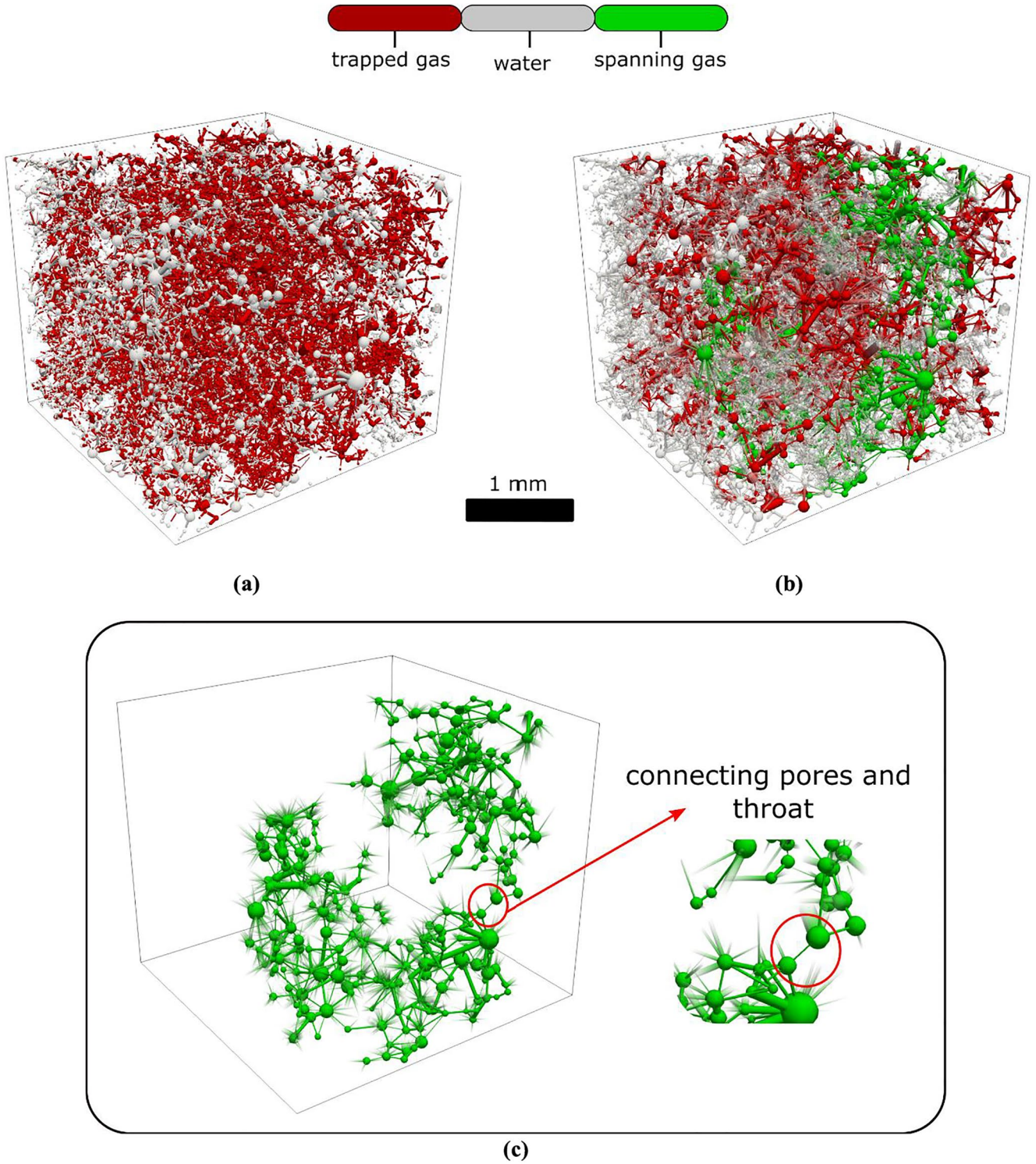

Figure 9. Visualization of gas-phase occupancy in the Heletz pore-network: (a) when originally trapped (the beginning of depletion simulation), (b) when the gas is first flowing (remobilization), (c) spanning gas cluster (shown in green)—connected to both inlet (bottom) and outlet (top) of the network.

Looking at the gas relative permeabilities of both networks, a couple of features could be identified. Of particular importance are the trends observed for the depletion relative permeability. For both networks, the relative permeability to gas increases slowly even for the saturations beyond the critical saturation. The maximum gas relative permeability is also reduced significantly compared to that achieved at the end of primary drainage. This means that even when reconnected, the gas can only flow slowly.

A second important observation is that the imbibition relative permeability is slightly higher than the corresponding drainage curve over a range of saturations. This behavior, which is a characteristic of a strongly water-wet medium, can be explained as follows. The CO_2, as the non-wetting phase, fills the largest pores while water, as the wetting phase, resides at the narrowest throats and corners of the pores. Toward the end of drainage, many CO_2 filled pores are only connected to a single pore that is also occupied by CO_2. These dead-end pores do not contribute to the flow, though may host a large volume of the non-wetting phase. During imbibition pore-filling is most favored in pores that have neighboring CO_2 filled pores—the dead-end pores occupied by CO_2 (Spiteri et al., 2008). Although this results in a significant reduction in CO_2 saturation, it leads to a small decrease in CO_2 relative permeability. Thereafter, snap-off dominates leading to significant trapping, with a large reduction in CO_2 relative permeability (Spiteri et al., 2008). This type of competition gives the hysteresis trend seen in Figure 8. Another characteristic feature that can be seen in Figure 8 is that the imbibition k_{rg} declines to zero sharply close to S_{gr}, as the final connected pathways of the gas are disconnected (Blunt, 2017).

The results are assumed to be insensitive to the rate at which pressure declines: (a) we assume that the rate is sufficiently slow to allow the concentration to reach equilibrium at the pore scale; and (b) we do not allow the nucleation of new bubbles in our model for the reasons described in Section 2.3. As reported in earlier studies (Kamath & Boyer, 1995), low pressure decline rates have no substantial effect on S_{gc}. However, there are a number of studies that have reported an increasing or even a non-monotonic trend of S_{gc} versus increasing pressure decline rate, particularly where the rate is high. This discrepancy can be attributed mainly to the way we interpret and determine S_{gc} (Li & Yortsos, 1995a, 1995b; Tsimpanogiannis & Yortsos, 2004).

5. Conclusions

In this work, the remobilization of residually trapped gas due to pressure depletion is studied using pore network modeling, in the context of geological CO_2 storage. Our results provide important insights into the physics relevant to remobilization phenomenon, the main points of which can be summarized as follows.

- Both the mobilization saturation (S_{gmob}) and the rate of the relative permeability increase after remobilization and are affected by the depletion process, through an interplay between the various pore-scale mobilization mechanisms, namely diffusion, gas growth, and migration.
- Ostwald ripening affects gas phase reconnection, and in turn the critical gas saturation, but the effect is small. Higher S_{gmob} values considering Ostwald ripening suggest that the process of gas phase reconnection is delayed due to the redistribution of gas bubbles. This is a safety enhancing phenomenon in the context of CO_2 storage. The effects of Ostwald ripening on the depletion gas relative permeability are insignificant.
- The gravitational force had a negligible effect on the remobilization of the residually trapped CO_2, meaning that while residual trapping could be thermodynamically unstable, it is hydrodynamically stable.
- Under depletion conditions, the gas relative permeability increases very slowly, even for saturations beyond the critical gas saturation. This observation adds to the security of geological CO_2 trapping in cases where the mobilization of trapped CO_2 under depletion conditions is of concern.

Although we attempted to address the most important mechanisms involved in this phenomenon, certain assumptions were also made. Considering this and the fact that remobilization of residually trapped CO_2 under pressure depletion is not very well understood, we suggest that further research focuses on investigating the role of pressure depletion rate, high viscous and gravity forces, as well as the effects of geometrical network properties, initial water saturation, and contact angle on remobilization. The results of the current study are consistent with our earlier field-scale observations from Heletz CO_2 injection experiments, both in terms of the value of the remobilization saturation and the general behavior (Moghadasi et al., 2022). This reveals important implications of our results for security assessment of residual trapping in CO_2 storage.

Data Availability Statement

Pore-network simulator used in this study, numSCAL, was originally developed at Heriot-Watt University, UK. A basic version of numSCAL is available at https://github.com/ahboujelben/numSCAL-basic. The repository also provides an introduction on the code, licensing, resources and prerequisites. An access to the full version can be obtained by contacting Prof Steven McDougall at Hertiot-Watt University. Micro-CT image and network of Bentheimer sandstone is deposited at Pore-Scale Modelling Research Group at Imperial College webpage and are available via https://www.imperial.ac.uk/earth-science/research/research-groups/pore-scale-modelling/micro-ct-images-and-networks/. Dataset for Heletz sandstone is available in a data repository (Zenodo) via https://doi.org/10.5281/zenodo.7675085.

Acknowledgments
The research leading to these results has received funding from Swedish Energy Agency (Energimyndigheten) [Grant 435261]. The computations were performed on resources provided by SNIC through Uppsala Multidisciplinary Center for Advanced Computational Science (UPPMAX) under projects SNIC [2020/5–571, 2022-22-16]. We would also like to thank specifically Dr. Pavlin Mitev from UPPMAX for his great help with computational resources.

References

Ahmed, T., Evans, J., Kwan, R., & Vivian, T. (1998). Wellbore liquid blockage in gas-condensate reservoirs. In *SPE eastern regional meeting*. OnePetro. https://doi.org/10.2118/51050-ms

Al-Masri, W., & Shapiro, A. (2021). Experimental determination of relative permeabilities and critical gas saturations under solution-gas drive. *Journal of Petroleum Science and Engineering*, *202*, 108509. https://doi.org/10.1016/j.petrol.2021.108509

Amili, P., & Yortsos, Y. C. (2006). Darcian dynamics: A new approach to the mobilization of a trapped phase in porous media. *Transport in Porous Media*, *64*(1), 25–49. https://doi.org/10.1007/s11242-005-1397-y

Andrew, M., Bijeljic, B., & Blunt, M. J. (2014). Pore-by-pore capillary pressure measurements using X-ray microtomography at reservoir conditions: Curvature, snap-off, and remobilization of residual CO2. *Water Resources Research*, *50*(11), 8760–8774. https://doi.org/10.1002/2014wr015970

Azin, R., Mahmoudy, M., Raad, S. M. J., & Osfouri, S. (2013). Measurement and modeling of CO_2 diffusion coefficient in Saline Aquifer at reservoir conditions. *Central European Journal of Engineering*, *3*(4), 585–594. https://doi.org/10.2478/s13531-012-0069-2

Bagudu, U., McDougall, S. R., & Mackay, E. J. (2015). Pore-to-Core-Scale network modelling of CO_2 migration in porous media. *Transport in Porous Media*, *110*(1), 41–79. https://doi.org/10.1007/s11242-015-0556-z

Bagudu, U., McDougall, S. R., & Mackay, E. J. (2018). Network modelling analysis of a depressurization experiment on a North Sea reservoir core sample. *Journal of Petroleum Science and Engineering*, *162*, 63–75. https://doi.org/10.1016/j.petrol.2017.11.036

Basirat, F., Yang, Z., Bensabat, J., Levchenko, S., Pan, L., & Niemi, A. (2020). Characterization of CO_2 self-release during Heletz Residual Trapping Experiment I (RTE I) using a coupled wellbore-reservoir simulator. *International Journal of Greenhouse Gas Control*, *102*, 103162. https://doi.org/10.1016/j.ijggc.2020.103162

Berg, S., Gao, Y., Georgiadis, A., Brussee, N., Coorn, A., Van der Linde, H., et al. (2020). Determination of critical gas saturation by micro-CT. *Petrophysics*, *61*(02), 133–150. https://doi.org/10.30632/pjv61n2-2020a1

Blunt, M. J. (2001). Flow in porous media—Pore-network models and multiphase flow. *Current Opinion in Colloid & Interface Science*, *6*(3), 197–207. https://doi.org/10.1016/s1359-0294(01)00084-x

Blunt, M. J. (2017). *Multiphase flow in permeable media: A pore-scale perspective*. Cambridge university press.

Bondino, I., McDougall, S. R., & Hamon, G. (2002). Pore network modelling of heavy oil depressurisation: A parametric study of factors affecting critical gas saturation and 3-phase relative permeabilities. In *SPE international thermal operations and heavy oil symposium and international horizontal well technology conference*. Society of Petroleum Engineers. https://doi.org/10.2118/78976-ms

Bondino, I., McDougall, S. R., & Hamon, G. (2003). Interpretation of a long core heavy oil depletion experiment using pore network modelling techniques. In *International Symposium of the Society of core Analysts*.

Boujelben, A. H. (2017). *A new pore-scale numerical simulator for investigating special core analysis data*. Heriot-Watt University.

Cadogan, S. P., Maitland, G. C., & Trusler, J. P. M. (2014). Diffusion coefficients of CO_2 and N_2 in water at temperatures between 298.15 K and 423.15 K at pressures up to 45 MPa. *Journal of Chemical & Engineering Data*, *59*(2), 519–525. https://doi.org/10.1021/je401008s

De Chalendar, J. A., Garing, C., & Benson, S. M. (2018). Pore-scale modelling of Ostwald ripening. *Journal of Fluid Mechanics*, *835*, 363–392. https://doi.org/10.1017/jfm.2017.720

Drummond, A., Fishlock, T., Naylor, P., & Rothkopf, B. (2001). An evaluation of post-waterflood depressurisation of the south Brae field, North Sea. In *SPE annual technical conference and exhibition*. Society of Petroleum Engineers. https://doi.org/10.2118/71487-ms

Egermann, P., Schaaf, T., & Bréfort, B. (2010). A modified hysteresis relative permeability including a gas remobilization threshold for better production forecasts of gas storages. *Petrophysics*, *51*(05).

Egermann, P., & Vizika, O. (2000). Critical gas saturation and relative permeability during depressurization in the far field and the near-wellbore region. In *SPE annual technical conference and exhibition*. Society of Petroleum Engineers. https://doi.org/10.2118/63149-ms

Ezeuko, C. C., McDougall, S. R., Bondino, I., & Hamon, G. (2010). Dynamic pore-network simulator for modeling buoyancy-driven migration during depressurization of oil-saturated systems. *SPE Journal*, *15*(04), 906–916. https://doi.org/10.2118/117479-pa

Fevang, Ø., & Whitson, C. H. (1996). Modeling gas-condensate well deliverability. *SPE Reservoir Engineering*, *11*(04), 221–230. https://doi.org/10.2118/30714-pa

Fishlock, T. P., Smith, R. A., Soper, B. M., & Wood, R. W. (1988). Experimental studies on the waterflood residual gas saturation and its production by Blowdown. *SPE Reservoir Engineering*, *3*(02), 387–394. https://doi.org/10.2118/15455-PA

Garing, C., De Chalendar, J. A., Voltolini, M., Ajo-Franklin, J. B., & Benson, S. M. (2017). Pore-scale capillary pressure analysis using multi-scale X-ray micromotography. *Advances in Water Resources*, *104*, 223–241. https://doi.org/10.1016/j.advwatres.2017.04.006

Gershenzon, N. I., Soltanian, M., Ritzi, R. W., & Dominic, D. F. (2014). Influence of small scale heterogeneity on CO_2 trapping processes in deep saline aquifers. *Energy Procedia*, *59*, 166–173. https://doi.org/10.1016/j.egypro.2014.10.363

Huber, E. J., Stroock, A. D., & Koch, D. L. (2018). Modeling the dynamics of remobilized CO_2 within the geologic subsurface. *International Journal of Greenhouse Gas Control*, *70*, 128–145. https://doi.org/10.1016/j.ijggc.2018.01.020

IPCC. (2005). *Carbon dioxide capture and storage. Special Report*. Cambridge University Press.

Jiang, P., Li, X., Xu, R., Wang, Y., Chen, M., Wang, H., & Ruan, B. (2014). Thermal modeling of CO_2 in the injection well and reservoir at the Ordos CCS demonstration project, China. *International Journal of Greenhouse Gas Control*, *23*, 135–146. https://doi.org/10.1016/j.ijggc.2014.01.011

Joodaki, S., Moghadasi, R., Basirat, F., Yang, Z., Bensabat, J., & Niemi, A. (2020). Model analysis of CO_2 residual trapping from single-well push pull test—Heletz, residual trapping experiment II. *International Journal of Greenhouse Gas Control*, *101*, 103134. https://doi.org/10.1016/j.ijggc.2020.103134

Kamath, J., & Boyer, R. E. (1995). Critical gas saturation and supersaturation in low-permeability rocks. *SPE Formation Evaluation*, *10*(04), 247–253. https://doi.org/10.2118/26663-pa

Krevor, S., Blunt, M. J., Benson, S. M., Pentland, C. H., Reynolds, C., Al-Menhali, A., & Niu, B. (2015). Capillary trapping for geologic carbon dioxide storage—From pore scale physics to field scale implications. *International Journal of Greenhouse Gas Control*, *40*, 221–237. https://doi.org/10.1016/j.ijggc.2015.04.006

Lenormand, R., & Zarcone, C. (1984). Role of roughness and edges during imbibition in square capillaries. In *SPE annual technical conference and exhibition*. OnePetro. https://doi.org/10.2118/13264-ms

Li, X., & Yortsos, Y. C. (1995a). Theory of multiple bubble growth in porous media by solute diffusion. *Chemical Engineering Science*, *50*(8), 1247–1271. https://doi.org/10.1016/0009-2509(95)98839-7

Li, X., & Yortsos, Y. C. (1995b). Visualization and simulation of bubble growth in pore networks. *AIChE Journal*, *41*(2), 214–222. https://doi.org/10.1002/aic.690410203

Li, Y., Orr, F. M., & Benson, S. M. (2021). *Long-term redistribution of residual gas due to non-convective Transport in the aqueous phase* (pp. 1–23). Transport in Porous Media.

Li, Z., Yuan, L., Sun, G., Lv, J., & Zhang, Y. (2021). Experimental determination of CO_2 diffusion coefficient in a brine-saturated core simulating reservoir condition. *Energies*, *14*(3), 540. https://doi.org/10.3390/en14030540

Lu, W., Guo, H., Chou, I.-M., Burruss, R. C., & Li, L. (2013). Determination of diffusion coefficients of carbon dioxide in water between 268 and 473 K in a high-pressure capillary optical cell with in situ Raman spectroscopic measurements. *Geochimica et Cosmochimica Acta*, *115*, 183–204. https://doi.org/10.1016/j.gca.2013.04.010

McDougall, S. R., & Sorbie, K. S. (1999). Estimation of critical gas saturation during pressure depletion in virgin and waterflooded reservoirs. *Petroleum Geoscience*, *5*(3), 229–233. https://doi.org/10.1144/petgeo.5.3.229

Mehmani, Y., & Xu, K. (2022). Pore-network modeling of Ostwald ripening in porous media: How do trapped bubbles equilibrate? *Journal of Computational Physics*, 111041. https://doi.org/10.1016/j.jcp.2022.111041

Moghadasi, R., Basirat, F., Bensabat, J., Doughty, C., & Niemi, A. (2022). Role of critical gas saturation in the interpretation of a field scale CO_2 injection experiment. *International Journal of Greenhouse Gas Control*, *115*, 103624. https://doi.org/10.1016/j.ijggc.2022.103624

Moghadasi, R., Basirat, F., Bensabat, J., Doughty, C., & Niemi, A. P. (2020). Role of critical saturation in evaluating residual trapping in a field scale CO_2 injection experiment. *AGU Fall Meeting Abstracts*, *2020*, GC097–0003.

Naylor, P., Fishlock, T., Mogford, D., & Smith, R. (2000). Relative permeability measurements for post-waterflood depressurisation of the Miller field, North Sea. In *SPE annual technical conference and exhibition*. OnePetro. https://doi.org/10.2118/63148-ms

Niemi, A., Bear, J., & Bensabat, J. (2017). *Geological storage of CO_2 in deep saline formations* (Vol. 29). Springer.

Niemi, A., Bensabat, J., Joodaki, S., Basirat, F., Hedayati, M., Yang, Z., et al. (2020). Characterizing CO_2 residual trapping in-situ by means of single-well push-pull experiments at Heletz, Israel, pilot injection site–experimental procedures and results of the experiments. *International Journal of Greenhouse Gas Control*, *101*, 103129. https://doi.org/10.1016/j.ijggc.2020.103129

Niemi, A., Bensabat, J., Shtivelman, V., Edlmann, K., Gouze, P., Luquot, L., et al. (2016). Heletz experimental site overview, characterization and data analysis for CO_2 injection and geological storage. *International Journal of Greenhouse Gas Control*, *48*, 3–23. https://doi.org/10.1016/j.ijggc.2015.12.030

Øren, P.-E., Bakke, S., & Arntzen, O. J. (1998). Extending predictive capabilities to network models. *SPE Journal*, *3*(04), 324–336. https://doi.org/10.2118/52052-pa

Orr, F. M., Jr. (2018). Carbon capture, utilization, and storage: An update. *SPE Journal*, *23*(06), 2–444. https://doi.org/10.2118/194190-pa

Pore-Scale Modelling Research Group. Micro-CT images and networks. [Dataset] Retrieved from https://www.imperial.ac.uk/earth-science/research/research-groups/pore-scale-modelling/micro-ct-images-and-networks/

Qi, R., Laforce, T. C., & Blunt, M. J. (2009). Design of carbon dioxide storage in aquifers. *International Journal of Greenhouse Gas Control*, *3*(2), 195–205. https://doi.org/10.1016/j.ijggc.2008.08.004

Raghavan, R., & Jones, J. R. (1996). Depletion performance of gas-condensate reservoirs. *Journal of Petroleum Technology*, *48*(08), 725–731. https://doi.org/10.2118/36352-jpt

Ramstad, T., Berg, C. F., & Thompson, K. (2019). Pore-scale simulations of single-and two-phase flow in porous media: Approaches and applications. *Transport in Porous Media*, *130*(1), 77–104. https://doi.org/10.1007/s11242-019-01289-9

Rasmusson, K., Rasmusson, M., Tsang, Y., Benson, S., Hingerl, F., Fagerlund, F., & Niemi, A. (2018). Residual trapping of carbon dioxide during geological storage—Insight gained through a pore-network modeling approach. *International Journal of Greenhouse Gas Control*, *74*(April), 62–78. https://doi.org/10.1016/j.ijggc.2018.04.021

Shi, J.-Q., Imrie, C., Sinayuc, C., Durucan, S., Korre, A., & Eiken, O. (2013). Snøhvit CO_2 storage project: Assessment of CO_2 injection performance through history matching of the injection well pressure over a 32-months period. *Energy Procedia*, *37*, 3267–3274. https://doi.org/10.1016/j.egypro.2013.06.214

Spiteri, E. J., Juanes, R., Blunt, M. J., & Orr, F. M. (2008). A new model of trapping and relative permeability hysteresis for all wettability characteristics. *SPE Journal*, *13*(03), 277–288. https://doi.org/10.2118/96448-pa

Tanino, Y., & Blunt, M. J. (2012). Capillary trapping in sandstones and carbonates: Dependence on pore structure. *Water Resources Research*, *48*(8), 1–13. https://doi.org/10.1029/2011WR011712

Tatomir, A. B., Halisch, M., Duschl, F., Peche, A., Wiegand, B., Schaffer, M., et al. (2016). An integrated core-based analysis for the characterization of flow, transport and mineralogical parameters of the Heletz pilot CO_2 storage site reservoir. *International Journal of Greenhouse Gas Control*, *48*, 24–43. https://doi.org/10.1016/j.ijggc.2016.01.030

Tsimpanogiannis, I. N., & Yortsos, Y. C. (2002). Model for the gas evolution in a porous medium driven by solute diffusion. *AIChE Journal*, *48*(11), 2690–2710. https://doi.org/10.1002/aic.690481126

Tsimpanogiannis, I. N., & Yortsos, Y. C. (2004). The critical gas saturation in a porous medium in the presence of gravity. *Journal of Colloid and Interface Science*, *270*(2), 388–395. https://doi.org/10.1016/j.jcis.2003.09.036

Xu, K., Mehmani, Y., Shang, L., & Xiong, Q. (2019). Gravity-induced bubble ripening in porous media and its impact on capillary trapping stability. *Geophysical Research Letters*, *46*(23), 13804–13813. https://doi.org/10.1029/2019gl085175

Zuo, L., Krevor, S., Falta, R. W., & Benson, S. M. (2012). An experimental study of CO_2 exsolution and relative permeability measurements during CO_2 saturated water depressurization. *Transport in Porous Media*, *91*(2), 459–478. https://doi.org/10.1007/s11242-011-9854-2

Zuo, L., Zhang, C., Falta, R. W., & Benson, S. M. (2013). Micromodel investigations of CO_2 exsolution from carbonated water in sedimentary rocks. *Advances in Water Resources*, *53*, 188–197. https://doi.org/10.1016/j.advwatres.2012.11.004

References From the Supporting Information

Batzle, M., & Wang, Z. (1992). Seismic properties of pore fluids. *Geophysics*, *57*(11), 1396–1408. https://doi.org/10.1190/1.1443207

Chalbaud, C., Robin, M., Lombard, J.-M., Bertin, H., & Egermann, P. (2010). Brine/CO_2 interfacial properties and effects on CO_2 storage in deep saline aquifers. *Oil & Gas Science and Technology–Revue de l'Institut Français Du Pétrole*, *65*(4), 541–555. https://doi.org/10.2516/ogst/2009061

Duan, Z., Møller, N., & Weare, J. H. (1992). An equation of state for the CH_4-CO_2-H_2O system: I. Pure systems from 0 to 1000 C and 0 to 8000 bar. *Geochimica et Cosmochimica Acta*, *56*(7), 2605–2617. https://doi.org/10.1016/0016-7037(92)90347-l

Duan, Z., Sun, R., Zhu, C., & Chou, I.-M. (2006). An improved model for the calculation of CO_2 solubility in aqueous solutions containing Na+, K+, Ca2+, Mg2+, Cl−, and SO42. *Marine Chemistry*, *98*(2–4), 131–139. https://doi.org/10.1016/j.marchem.2005.09.001

Duan, Z., Hu, J., Li, D., & Mao, S. (2008). Densities of the CO_2–H_2O and CO_2–H_2O–NaCl systems up to 647 K and 100 MPa. *Energy & Fuels*, *22*(3), 1666–1674. https://doi.org/10.1021/ef700666b

Li, D., Graupner, B. J., & Bauer, S. (2011). A method for calculating the liquid density for the CO_2–H_2O–NaCl system under CO_2 storage condition. *Energy Procedia*, *4*, 3817–3824. https://doi.org/10.1016/j.egypro.2011.02.317

McBride-Wright, M. (2014). Viscosity and density of aqueous fluids with dissolved CO_2.

Ouyang, L.-B. (2011). New correlations for predicting the density and viscosity of supercritical carbon dioxide under conditions expected in carbon capture and sequestration operations. *The Open Petroleum Engineering Journal*, *4*(1), 13–21. https://doi.org/10.2174/1874834101104010013

Pitzer, K. S., Peiper, J. C., & Busey, R. H. (1984). Thermodynamic properties of aqueous sodium chloride solutions. *Journal of Physical and Chemical Reference Data*, *13*(1), 1–102. https://doi.org/10.1063/1.555709

Redlich, O., & Kwong, J. N. S. (1949). On the thermodynamics of solutions. V. An equation of state. Fugacities of gaseous solutions. *Chemical Reviews*, *44*(1), 233–244. https://doi.org/10.1021/cr60137a013

Soave, G. (1993). 20 years of Redlich-Kwong equation of state. *Fluid Phase Equilibria*, *82*, 345–359. https://doi.org/10.1016/0378-3812(93)87158-w

Spycher, N., Pruess, K., & Ennis-King, J. (2003). CO_2-H_2O mixtures in the geological sequestration of CO_2. I. Assessment and calculation of mutual solubilities from 12 to 100 C and up to 600 bar. *Geochimica et Cosmochimica Acta*, *67*(16), 3015–3031. https://doi.org/10.1016/s0016-7037(03)00273-4

Tsonopoulos, C., & Heidman, J. L. (1985). From Redlich-Kwong to the present. *Fluid Phase Equilibria*, *24*(1–2), 1–23. https://doi.org/10.1016/0378-3812(85)87034-5